ADVANCED MATERIALS
www.advmat.de

Controlled Electronic and Magnetic Landscape in Self-Assembled Complex Oxide Heterostructures

Dae-Sung Park, Aurora Diana Rata, Rasmus Tindal Dahm, Kanghyun Chu, Yulin Gan, Igor Maznichenko, Sergey Ostanin, Felix Trier, Hionsuck Baik, Woo Seok Choi, Chel-Jong Choi, Young Heon Kim, Gregory Jon Rees, Hafliði Pétur Gíslason, Paweł Adam Buczek, Ingrid Mertig, Mihai Adrian Ionescu, Arthur Ernst, Kathrin Dörr, Paul Muralt, and Nini Pryds*

Complex oxide heterointerfaces contain a rich playground of novel physical properties and functionalities, which give rise to emerging technologies. Among designing and controlling the functional properties of complex oxide film heterostructures, vertically aligned nanostructure (VAN) films using a self-assembling bottom-up deposition method presents great promise in terms of structural flexibility and property tunability. Here, the bottom-up self-assembly is extended to a new approach using a mixture containing a 2Dlayer-by-layer film growth, followed by a 3D VAN film growth. In this work, the two-phase nanocomposite thin films are based on $LaAlO_3$:$LaBO_3$, grown on a lattice-mismatched $SrTiO_{3001}$ (001) single crystal. The 2D-to-3D transient structural assembly is primarily controlled by the composition ratio, leading to the coexistence of multiple interfacial properties, 2D electron gas, and magnetic anisotropy. This approach provides multidimensional film heterostructures which enrich the emergent phenomena for multifunctional applications.

1. Introduction

Over the last three decades, the rapid and continued development of thin film growth technologies of strongly correlated complex oxides (e.g., those composed of transition metals with the variable occupancy of *d*-/*f*-band electrons and/or with orbital orderings) provide rich and emerging functionalities such as high-mobility 2D electron gases (2DEGs),[1] ionic conduction,[2] topological states,[3] ferroelectricity,[4] ferromagnetism,[5] and multiferroicity.[4,6,7] These functionalities represent properties different from their bulk counterparts. The prototypical heterostructure, $LaAlO_3$(LAO)/$SrTiO_3$(STO), is an excellent example that exhibits a wealth of intriguing properties at the interface such as low-temperature

D.-S. Park, K. Chu, P. Muralt
Institute of Materials
Swiss Federal Institute of Technology–EPFL
Lausanne 1015, Switzerland
E-mail: daepa@dtu.dk

D.-S. Park, R. T. Dahm, F. Trier, N. Pryds
Department of Energy Conversion and Storage
Technical University of Denmark
Kgs Lyngby DK-2800, Denmark

D.-S. Park, M. A. Ionescu
Institute of Electrical and Micro Engineering
Swiss Federal Institute of Technology–EPFL
Lausanne 1015, Switzerland

A. D. Rata, I. Maznichenko, S. Ostanin, I. Mertig, K. Dörr
Institut für Physik
Martin-Luther-Universität Halle-Wittenberg
06099 Halle, Germany

The ORCID identification number(s) for the author(s) of this article can be found under https://doi.org/10.1002/adma.202300200

DOI: 10.1002/adma.202300200

Y. Gan
Institute of Physics
Chinese Academy of Sciences
Beijing 100190, P. R. China

H. Baik
Korea Basic Science Institute
Seoul 02841, Republic of Korea

W. S. Choi
Department of Physics
Sungkyunkwan University
Suwon 16419, Republic of Korea

C.-J. Choi
School of Semiconductor and Chemical Engineering
Chonbuk National University
Jeonju 54596, Republic of Korea

Y. H. Kim
Graduate School of Analytical Science and Technology
Chungnam National University
Daejeon 34134, Republic of Korea

G. J. Rees
Department of Materials
University of Oxford
Oxford OX1 3PH, UK

superconductivity (below ≈200 mK) and unconventional magnetism.[8,9] The low-dimensional conduction stems from the confined charge carriers at the polar/non-polar complex oxide interface and appears when ≥ 4 unit cells (UCs) of LAO are grown on singly terminated TiO_2-STO substrates.[10] Despite the continuous debate to the underlying mechanism on the enhanced electron mobility at the interfaces, these interfaces turn out to be a central way to realize high electron mobility ($\mu \approx 1000 - 10000$ cm^2 V^{-1} s^{-1} at 2 K). It is widely believed that realizing interfaces with high mobility requires delicate growth control to achieve the interfacial electron and/or orbital reconstruction, control of oxygen vacancy content, cation stoichiometry, and sufficiency of charge carrier sources.[11–14] The electronic and magnetic interactions at the 2DEGs have been exploited via electrical gating,[15,16] inserting δ-doping layers,[17] and assembly of magnetic and ferroelectric layers[18,19] to trigger tunable functionalities for nanoscale electronic applications such as spin valves and non-volatile electrical switching devices.

Another approach for controlling the functional properties of complex oxide heterostructures is to utilize self-assembled 3D vertical arrays of heterointerfaces in VAN films by composing two or more different phases, which are largely mismatched under strain-mediated and/or different film growth modes.[20,21] In order to obtain distinct and well-separated pillars, VAN thin films were usually grown using targets that contain equal compositions of two oxide material components or alternatively, relatively high composition ratios of a secondary phase component to a host material one (e.g., 0.2 – 0.5).[20–24] The VAN film growth characteristics have been explored using materials components differing in crystallographic structure, thermal expansion, elastic constant, and strain relaxation during film growth. The growth of VAN films is typically driven by the different surface energy and wettability between two phases and a substrate. One oxide phase grows in layer-by-layer growth mode (Frank–Van der Merwe) to form a film matrix, while the other phase grows in island mode (Volmer–Weber). The latter leads to the formation of secondary nanopillars/nanocolumns embedded in the matrix. The main advantages of this approach are i) a self-assembly of vertical interfaces of two/more phase materials and ii) circumventing the length-scale and number limits of conventional planar epitaxial thin film heterointerfaces (e.g., superlattice-type heterostructures) for mesoscale-film materials. Thus, it can enrich the interfacial effects in terms of lattice strain, defect, charge, and spin. The main difference between the horizontal and vertical interfaces is their different stress configuration. The horizontal interfaces have often zero vertical stress, whereas in the plane the misfit stress is in general non-zero.[25] In a layered structure, the elastic energy increases with increasing the number of monolayers, leading to the formation of misfit dislocations and the following stress reduction along the film. In contrast, the strain at the vertical interfaces is often accomplished by embedding a secondary oxide phase into the host matrix. Vertically aligned interfaces have shown fascinating multifunctional properties such as high ionic conductivity,[26] extraordinary ferroelectric orderings,[27] and magnetic anisotropy.[7] For example, high ionic conduction is preferentially formed near or at the vertical interfaces due to the formation of charged cation/anion point defects, e.g. oxygen vacancies at these interfaces.[21] Despite a large diversity of the functional properties, the formation of self-assembled vertical interfaces still relies on the growth of vertically aligned nanostructures which significantly limits the long-range electronic interactions due to the lack of long-range atomic precision between the two phases and the detrimental distribution of structural/atomic defects. In self-assembly approach, a mixture containing a layer-by-layer growth mode for 2D horizontal interface and a growth mode for 3D vertical interface is still not realized yet. Achieving such a film heterostructure can lead to the coexistence of multiple properties in two different interface orientations.

In this work, we demonstrate a new design of self-assembly multidimensional growth of 2D and 3D complex oxide nanocomposite thin films. The nanocomposite films are formed via a selection of two distinct oxide materials, rhombohedral $LaAlO_3$ [LAO(1-x)] and orthorhombic $LaBO_3$ [LBO(x)], outlined in **Figure 1**a. The composition of LAO:LBO (hereafter referred to as LABO) is varied over the range of LBO composition, $x = 0 - 10\%$. Our results show a structural transition from a 2D (LAO/STO) layered film to a 3D (LAO/LBO) vertical aligned nanopillar, which takes place at the composition above $x = 8\%$. The formation of these two distinct orientations of interfaces (horizontal and vertical interfaces) is achieved via a composition-assistant transition which is complementary with strain matching. This gives rise to simultaneous multiple properties such as 2DEG and perpendicular magnetic anisotropy in the multi-dimensional nanocomposite heterostructure.

2. Results and Discussion

2.1. Structural Transition of Epitaxial LABO Nanocomposite Films on STO

LABO composite thin films with composition of $0 \leq x \leq 10\%$ were simultaneously grown on TiO_2-terminated $SrTiO_3$(001) substrates by pulsed laser deposition (PLD) as schematically shown in Figure 1a. For a systematic comparison, the total thickness was kept constant at $t \approx 22–25$ nm. The composition of the grown films was determined by x-ray photoelectron spectroscopy (XPS) (Figure S1, Supporting Information). Details of the film growth are given in the Experimental Section.

To gain insights into the film growth characteristics of the LABO films, reciprocal space mappings (RSM) were performed

H. P. Gíslason
Science Institute
University of Iceland
Reykjavik IS-104, Iceland
P. A. Buczek
Department of Engineering and Computer Sciences
Hamburg University of Applied Sciences
20099 Hamburg, Germany
A. Ernst
Max-Planck-Institut für Mikrostrukturphysik
06120 Halle, Germany
A. Ernst
Institute of Theoretical Physics
Johannes Kepler University
Linz 4040, Austria

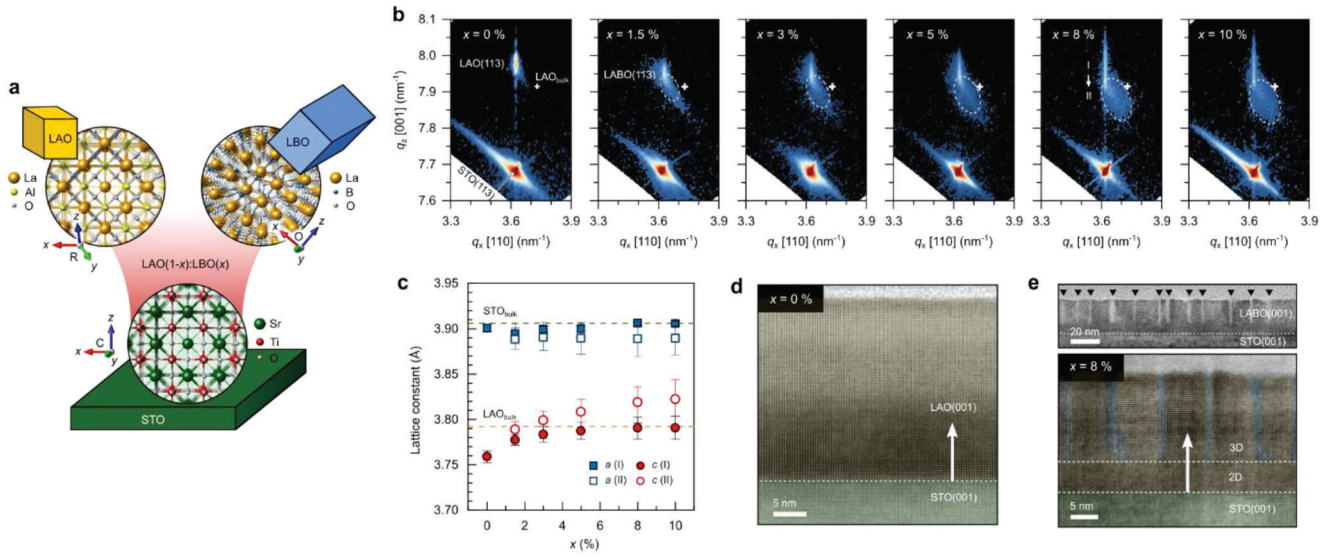

Figure 1. The growth of LABO nanocomposite films on STO(001) substrates with different x. a) A schematic for the formation of LABO nanocomposite films, consisting of a rhombohedral LAO(1-x) and an orthorhombic LBO(x), grown on a cubic STO(001). b) RSMs around the STO (113) reflection for the LABO(x = 0 – 10%)/STO samples. The cross mark indicates the $(113)_{pc}$ reflection position of bulk LAO (a_{pc} = 3.79 Å). A gradual separation of streak and broad peaks for the RSM$(113)_{pc}$ reflections of the nanocomposite films gradually is observed with increasing x. c) The a- and c-axis lattice constants of the nanocomposite films with different x. The lattice parameters of the (I) and (II) layers are separately presented. d) A cross-sectional HR-STEM image projected along <100> direction for the 25 nm-thick epitaxial LAO film grown on STO (001). e) Cross-sectional TEM (upper panel) and HR-STEM (lower panel) images of the LABO (x = 8%) nanocomposite film on STO (001). The results indicate the formation of a mixed LABO film structure, consisting of an initial epitaxial 2D layer and subsequent 3D vertically aligned nanocomposite layer, grown on STO (001).

around the STO(113) reflections. Figure 1b shows the results of the RSM. The RSM shows that the in-plane LAO(*hh*0) for the undoped LAO film (≈25 nm thick) is constrained along the STO(*hh*0) yielding a positive strain of ≈ +3.0%. The out-of-plane (00*l*) of the film shows a negative strain of ≈ −0.8% following the Poisson ratio, partially relaxing back toward the value of bulk LAO. In contrast, the RSM of the LABO nanocomposite films (22 – 25 nm thick) on STO(001) exhibits the development of two reflections of the films that vary significantly with the composition, *x*. These two reflections are assigned to: I) a film region that is coherently constrained to the in-plane STO and II) a region that moves away from the in-plane STO. The nanocomposite films with lower compositions ($x \leq 5\%$) indicate partial in-plane strain relaxation of the region-I with respect to STO while the region-II is gradually developed with higher compositions, *x*. When the composition increases above $x \geq 8\%$, the reflections of the $(113)_{pc}$ plane of the nanocomposite films separate into two regions, streak and broad peaks. The streak peak reflects the strain gradient of a 2D coherent film layer which is perfectly aligned along with the in-plane STO. The resulting *c*-lattice constant of the coherent layers in the films increases with *x*, while aligning along the in-plane of the underlying STO substrate, as shown in Figure 1c. Thus, the *c*-lattice strain distribution of the coherent layer (lined up along the in-plane of STO in reciprocal space in Figure 1b) is different, compared to the case of the elastic deformation of a coherent LAO layer which is completely imposed by STO substrate with a Poisson ratio of LAO (0.24).[28] Due to the misfit strain between LAO and STO, a pure elastic deformation of the LAO layer on STO is undertaken with a reduced LAO thickness (≤20 UCs).[28] This leads to the in-plane and out-of-plane strain of $\varepsilon_x = +3.03\%$ and $\varepsilon_z = -1.92\%$, respectively. However, in this work, we observed that the in-plane and out-of-plane strain of the coherent layer (I) in the nanocomposite ($x \geq 8\%$) films are $\varepsilon_x = +3.0\%$ and $\varepsilon_z = +0.1\%$ as compared with the bulk LAO value, respectively. This means that the out-of-plane of the coherent layer is oppositely constrained (*c*-axis lattice elongation) in the LABO nanocomposite films maintaining the in-plane matching with the underlying STO substrate.

A clear increase in the reflection area and the intensity of the broad reflection region-II is observed with higher compositions (see dashed line in Figure 1b). This is believed to be due to a strain relaxation process of the LAO phase, which is extended after the development of the region-I. Importantly, the position of the region II in RSM seems to shift away from the value of the bulk LAO (see Figure 1b). We further confirmed that the lattice of the region-II is distorted tetragonally. This was verified by RSM reflections for different crystallographic orientations of the films (Figure S2, Supporting Information). These results indicate a two-step structural development, i.e., an initial growth of coherent 2D layer and a following relaxed layer. When the composition of LBO reaches $x \geq 8\%$, the strain distribution of the LABO nanocomposite films is manifested. To confirm this structural assembly of the LABO films on the STO(001), scanning transmission electron microscopy (STEM) measurements were performed. Figure 1d illustrates a cross-sectional high-angle annular dark field (HAADF) STEM image of the undoped LAO(001) film grown on STO(001). As expected, for the undoped LAO ($x = 0$) (001) film grown on STO(001), only a layer-by-layer epitaxial growth was observed. Significant structural disorder was found in the LBO composition of $x \leq 5\%$ (Figure S3, Supporting Information). In contrast,

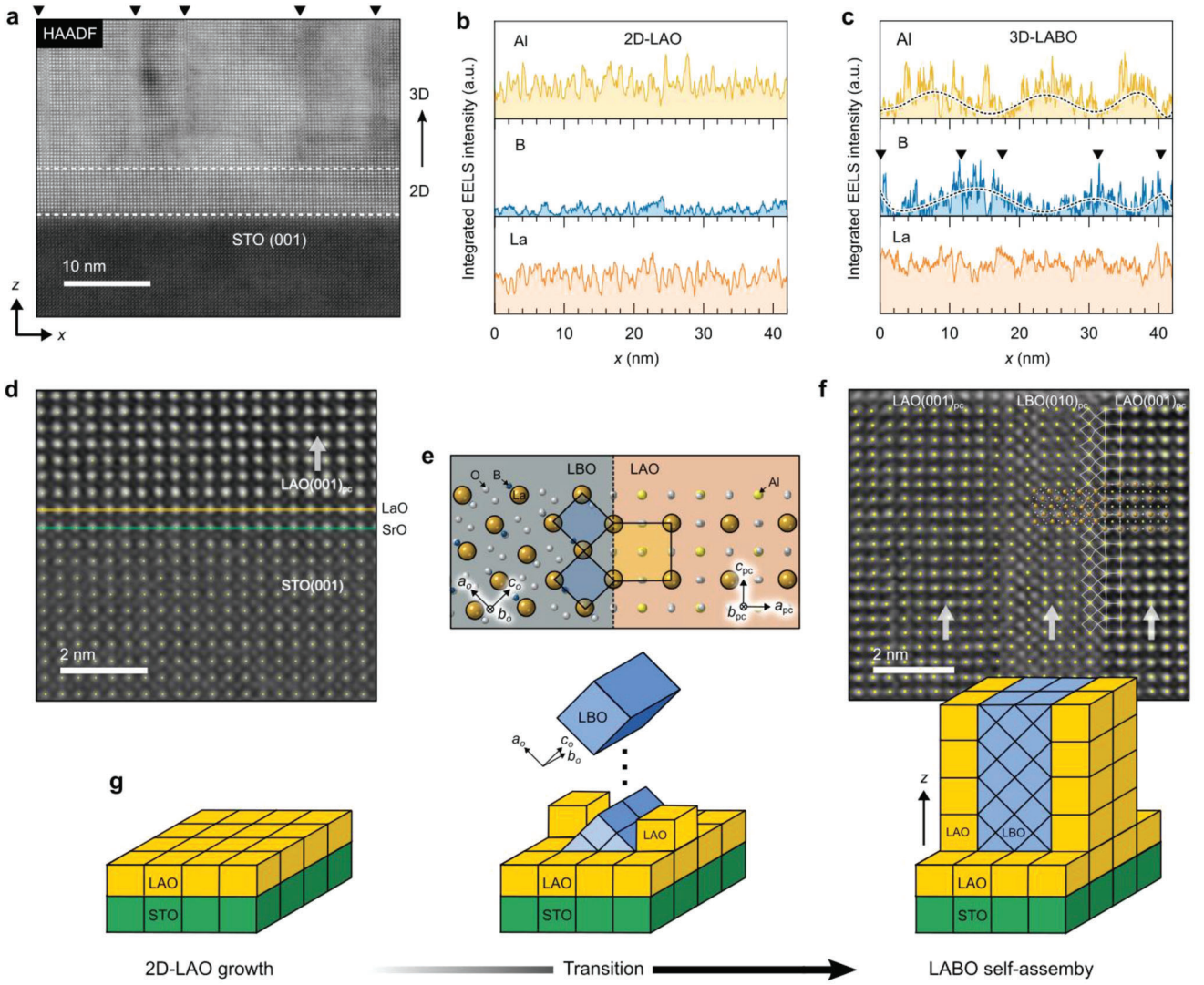

Figure 2. Formation of 2D–3D LABO film layers on STO(001). a) A cross-sectional HAADF-STEM image for a 2D–3D LABO(x = 10%)/STO(001) sample. The positions of vertical stripes in the 3D area are marked along the x-direction by triangles. b,c) Integrated EELS intensity profiles of Al, B, and La elements for the 2D (b) and 3D (c) areas corresponding to the film areas in (a). d) An atomic resolution HAADF-STEM image for the atomically abrupt 2D-LAO/STO interface in the LABO/STO heterostructure. e) Schematics for the crystallographic alignment of pseudocubic LAO and orthorhombic LBO crystals. f) The corresponding atomic resolution HAADF-STEM image for the vertically aligned LAO:LBO nanocomposite film layer. g) Schematic illustrations for the transient growth sequence of 2D–3D LABO nanocomposite film on STO.

we found that the LABO film ($x = 8\%$) shows well-defined vertically aligned nanostructures (1.5–2 nm width) with visible contrast (/atomic contrast) as shown in the HAADF-STEM images in Figure 1e. The ratio of the relatively dark to bright areas in the nanocomposite film layer is around $\approx 0.91 \pm 0.03$, similar to what observed in the composition of the nanocomposite film ($x = 8\%$). Interestingly, the vertically aligned structure is not directly formed on STO(001) substrate, but they developed after the initial 2D layer was formed (see Figure 1e). The TEM results verify the spontaneous occurrence of a two-step growth of the 2D layer and the subsequent 3D vertical array in the epitaxial LABO nanocomposite film, which is consistent with the XRD results.

2.2. Growth Mechanism of Self-Assembled 2D–3D LABO Nanocomposite Film Structure

To understand the compositional characteristics of the self-assembled LABO nanocomposite film, we carried out 2D elementary mappings for B, Al, La, and O for the 2D–3D LABO film ($x = 10\%$) using electron energy loss spectroscopy (EELS) as shown in **Figure 2**a and Figure S4 (Supporting Information). Figure 2b,c exhibits the integrated EELS intensities of Al, B, and La for the 2D and 3D film areas, respectively. The results indicate that the 2D layer is mainly composed of the Al and La contents with indistinguishable intensity of the B *K*-edge EELS signal. However, in the 3D film layer, B signals were found,

also confirmed by time-of-flight secondary ion mass spectroscopy (TOF-SIMS) (see Figure S5, Supporting Information). The intensity of B signal is alternated in the lateral direction with the Al intensity distribution. The intensity signal of the La is kept almost uniform in the lateral (x) and vertical (z) directions. The periodic distribution of B directly corresponds to the positions of vertical nanostructures in the 3D pillar-matrix layer as denoted in Figure 2a. An abrupt lateral interface is formed between the self-assembled 2D-LAO and STO (see Figure 2d). In the upper 3D nanocomposite film layer, the two vertically aligned LAO and LBO structures are tightly coupled through the vertical interfaces. We found that the lattice match between LAO and LBO phases occur via aligning the $LAO[100]_{pc}//LBO[010]_{pc}$ (or $LBO[-101]_{o}$) and $LAO[001]_{pc}//LBO[100]_{pc}$ as schematically illustrated in Figure 2e,f. Note that the $[101]_{o}$ and $[010]_{o}$ crystallographic orientations of orthorhombic LBO (space group: *Pnam*, $a_{o} = 5.106$ Å, $b_{o} = 8.257$ Å, and $c_{o} = 5.873$ Å) correspond to pseudocubic $[100]_{pc}$ and $[001]_{pc}$ directions, respectively.[29,30] Consequently, our results directly show that the consecutive formation of coherent 2D film layer and vertically arrayed 3D film is spontaneously formed in the LABO/STO(001) heterostructures (Figure 2g).

In general, the nucleation-and-growth process on a substrate relies on island formation which is controlled by temperature, the surface concentration of adatoms or molecular, ionic species, nucleation sites (e.g., substrate treatment, surface defects, dislocations), and growth rate.[22] When the concentration of boron in the LBO is low, the nucleation and the subsequent growth process (coalescence) are limited by a low probability of boron atoms to diffuse and form a critical nucleus (a critical nucleus is one that has the potential to grow), causing a random distribution of atomic point defects (solid solution). Alternatively, when the adatom concentration of boron is sufficiently high, i.e., when the LBO compositions of $x \geq 8\%$, a supersaturation condition is achieved,[25] leading to the nucleation of LBO crystals. This means that the nucleation and growth of LBO islands is promoted by high diffusivity/low capture rate of boron atoms on the LAO surface. The change of the film structure from a 2D layer to a 3D-VAN is accompanied by a relaxation process of the elastic energy that minimizes the misfit strain between LAO and STO for LBO formation in the nanocomposite film following the *Stranski–Krastnov* growth mode.[25] Choosing an equal composition (e.g., ratio of the LAO:LBO = 50:50) would lead to only the formation of VAN structure.[20,21] Overall, the growth processes can be described in the following way: i) the initial growth of 2D LAO on STO(001) under 3% biaxial strain with less boron accommodation, ii) strain relaxation after a critical thickness of ≈10 UC by overcoming the *Matthews–Blakeslee barrier*,[31] resulting in excessive boron diffusion toward the growing surface (in energetically favorable sites, e.g. edge dislocations), and iii) the accumulated concentration of boron distributed as islands to facilitate the nucleation of LBO on the 2D LAO surface, which leads to the growth of 3D vertically aligned LAO:LBO nanostructures. This transient growth behavior was directly monitored by in situ reflection high energy electron diffraction (RHEED) during the LABO film growth process when compared to the 2D growth feature of undoped LAO on STO (Figure S6, Supporting Information). Based on our proposed mechanism, the content of B in the 2D layer is very small, which was also qualitatively confirmed by TOF-SIMS (Figure S5, Supporting Information).

2.3. Epitaxial Strain Distribution in Multi-Dimensional LABO/STO(001) Heterostructure

In order to understand the strain distribution of the 2D–3D LABO/STO(001) heterostructure, we performed the peak-pair analysis and associated strain analysis from the STEM images. Details of the image processing (including noise filtering, intensity detection and refinement) are given in Figure S7 (Supporting Information). **Figure 3**a shows the refined HAADF-STEM image for a self-assembled 2D–3D LABO ($x = 10\%$) film layer on STO(001). Based on statistical determination of La cage with atomic precisions of ≈20 pm, lattice displacements and the associated epitaxial strain taken by the STEM image were elaborated using the lattice parameter (3.905 Å) of cubic bulk STO. Figure 3b,c exhibits strain maps for the relative biaxial (ε_{xx}) and uniaxial (ε_{zz}) strain of the 2D–3D LABO/STO heterostructure, revealing the strain characteristics along the x- and z-axis. The ε_{xx} mapping (Figure 3b) shows that the in-plane spacing of the 2D LAO layer is perfectly matched, as expected, with that of the underlying STO. In the 3D LABO layer, we observe an alternating strain characteristic along the lateral direction with the repetition of tensile (average $\varepsilon_{xx} \approx +3.5\%$ with respect to a of bulk STO) and compressive (average $\varepsilon_{xx} \approx -1\%$) strain. A displacement vector mapping for a transient LAO-to-LABO area presented in Figure 3d directly visualizes the opposite directions [100] and [−100] of the compressive strain of the two LAO columns across an LBO column. The aligned nanostructures (R1) with tensile strain correspond to the $(010)_{pc}$-oriented LBO crystals in the LABO composite film layer, while the areas (R2) with compressive strain correspond to the $(001)_{pc}$-oriented LAO columns. We found further that the out-of-plane compressive strain (ε_{zz}) of the LABO composite layer in the z-direction saturates starting from $\epsilon_{zz} \approx -4\%$ toward an average $\varepsilon_{zz} \approx -1.8\%$. Notably, the ε_{zz} strain becomes uniform along the lateral x-direction (see Figure 3c). This reveals that the vertical alignment of the LAO:LBO nanocomposite film layer is energetically stabilized via a lateral period of alternating tensile and compressive ε_{xx} strain components as a complementary in-plane strain matching.

Another interesting observation is the ε_{zz} distribution at the self-assembled LAO/STO interface (Figure 3f). A large interfacial strain of $\varepsilon_{zz} \approx +4\%$ appears at the topmost area (<2 nm) of STO. In contrast, an opposite strain of max. $\varepsilon_{zz} \approx -4\%$ at the initial growth of the 2D LAO layer (5 nm-thick) gradually decreases toward the interface with the LABO. Such unique reversal lattice distortions (the pseudomorphically c-contracted LAO and c-elongated STO) across the interface is driven by the energy cost of the epitaxially contracted LAO. This can lead to the emergence of an epitaxial strain-mediated head-to-head ferroelectric-like polarization and thus interfacial conductivity (similar to the formation of charged domain walls in the head-to-head (or tail-to-tail) domain configuration of insulating ferroelectrics).[32] Together with such reversal c-lattice distortions of LAO and topmost STO, 2DEG formation have been also observed in the STO of conductive LAO/STO heterosystems with a critical thickness of LAO (>3 unit cells).[33,34] Our observation is that such reversal lattice distortions across the interface are preserved in conjunction with the self-assembly of 2D–3D LABO film structure on STO(001).

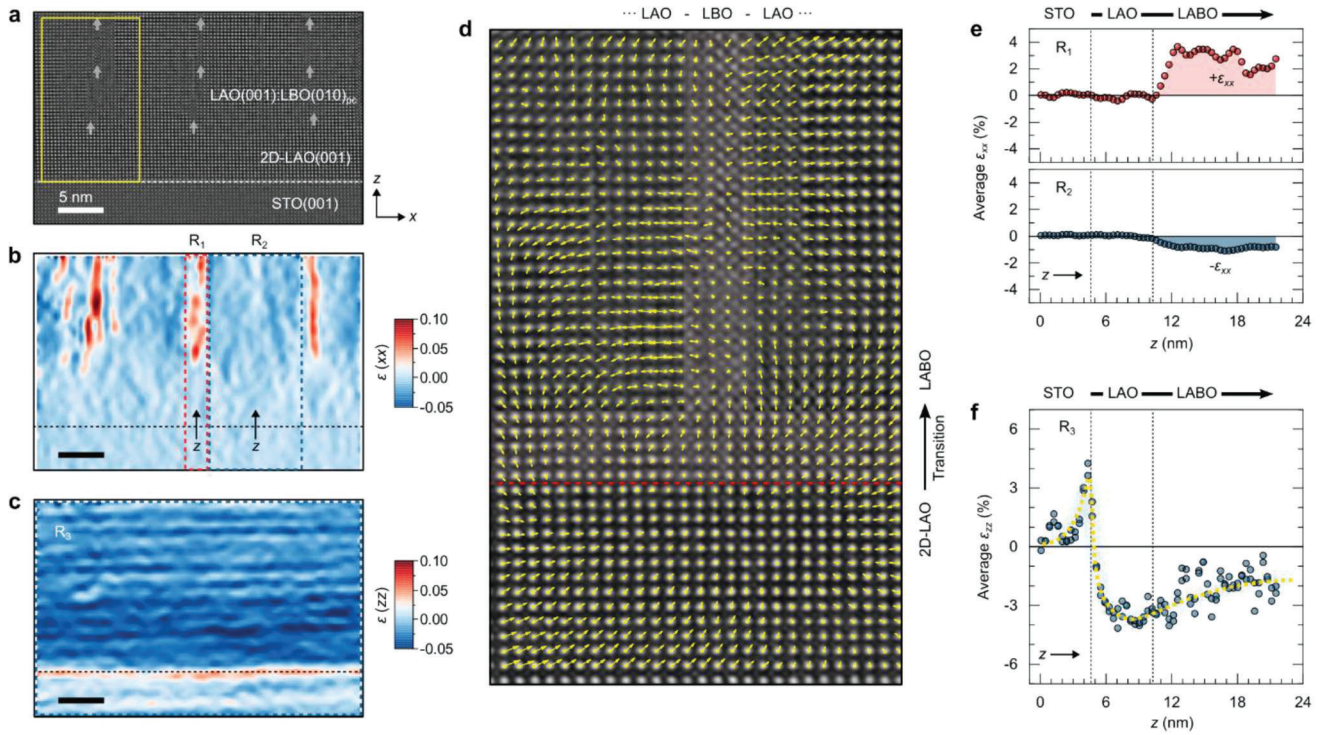

Figure 3. Strain distribution of the LABO/STO(001) heterostructure. a) The atomically refined STEM image for the 2D–3D LABO film on STO(001). b) The corresponding in-plane strain (ε_{xx}) map. c) The corresponding out-of-plane (ε_{zz}) map. d) Displacement vector map for the area where a structural transition starts from the topmost 2D layer, denoted by a red dash line. This selected area corresponds to the marked area in (A). In the intuitive quiver map, the reference mean lattice defines the starting point of individual arrows. e) The averaged ε_{xx} profiles along the *z*-direction for the LBO (R1 in (B)) and LAO (R2 in (B)) columns in the 3D LABO film layer. f) The averaged ε_{zz} profile along the *z*-direction of (a).

2.4. Formation of 2DEGs and Magnetism in the LABO/STO Heterostructures

Based on the above results, it is clear that two types of interfaces with different orientations (i.e., lateral and vertical interfaces) are formed. To probe the characteristics of the self-assembled 2D layer on the STO(001), photoluminescence (PL) measurements were performed using an excitation photon energy He-Cd laser (λ = 325 nm, 3.9 eV). **Figure 4**a shows the PL spectra, measured at 12 K, of a TiO_2-terminated STO(001) single crystal substrate used for film growth and the LABO ($0 \leq x \leq 10$)/TiO_2-STO samples. The PL emission of the samples were found with the near band-edge emission (BE) at ≈3.2 eV (close to the bandgap energy of STO, ≈3.2 eV). This is dominated by the recombination processes between the excited electrons and excited holes (conduction band minimum or subbands near the conduction band edges to valence band minimum).[35] The indirect bandgap STO substrate shows two weak BEs, commonly generated by the band-to-band optical transitions involving optical phonon absorption (BE-I at ≈3.27 eV) and excitation (BE-II at ≈3.22 eV). In contrast, for all the undoped LAO/STO and LABO/STO samples, additional BE emission pairs were found at lower energies, 3.18 – 3.20 eV (2DEG-I) and 3.25 – 3.26 eV (2DEG-II), compared to the BE-I and -II. Such a BE emission corresponds to the existence of 2D electron gases (2DEGs) at the heterointerfaces, consistent with an earlier work.[36] Thus, the energy and intensity of the 2DEG-associated BE directly reflects the band bending of the STO surface and the subsequent charge carrier confinement at the LABO/STO interfaces. A low-temperature PL feature of 2DEG is observed in the 25 nm-thick LAO/STO heterostructure. However, the BEs of the LABO($x \leq 5\%$)/STO heterostructures move toward lower energies with significant suppression. These degradations reflect the distorted/non-abrupt interfaces for the formation of 2DEGs. Notably, the enhancement of the phonon-assisted 2 DEG -emission pair was observed in the LABO ($x \geq 8\%$)/STO heterostructures at the same emission energies that appear in the undoped LAO/STO interface. This directly indicates the formation of a 2DEG LAO/STO interface in the 2D–3D LABO ($x \geq 8\%$) film structures. Furthermore, variable temperature BE emissions of the LABO ($x = 8\%$)/STO show a typical temperature-dependent characteristic of 2DEG formation (Figure 4b). To further identify and characterize the presence of a 2DEG at the LAO/STO interface in the heterostructures, electrical measurements with variable temperatures were performed. The undoped LAO/STO shows an insulating behavior at low temperatures (Figure 4d), although a signature of 2DEG was observed in PL. No data acquisition was available below 90 K due to the high resistance that exceeded the limit of measurement. This could be due to the fact that the carriers at the interface are localized and/or the absence of long-range conducting channel along the interface.[11,12] Moreover, the LABO/STO heterostructures with $x \leq 5\%$ were insulating due to the structural disorder and the lack of the 2D-LAO/STO interfaces, consistent with largely suppressed 2DEG emissions in PL. When the

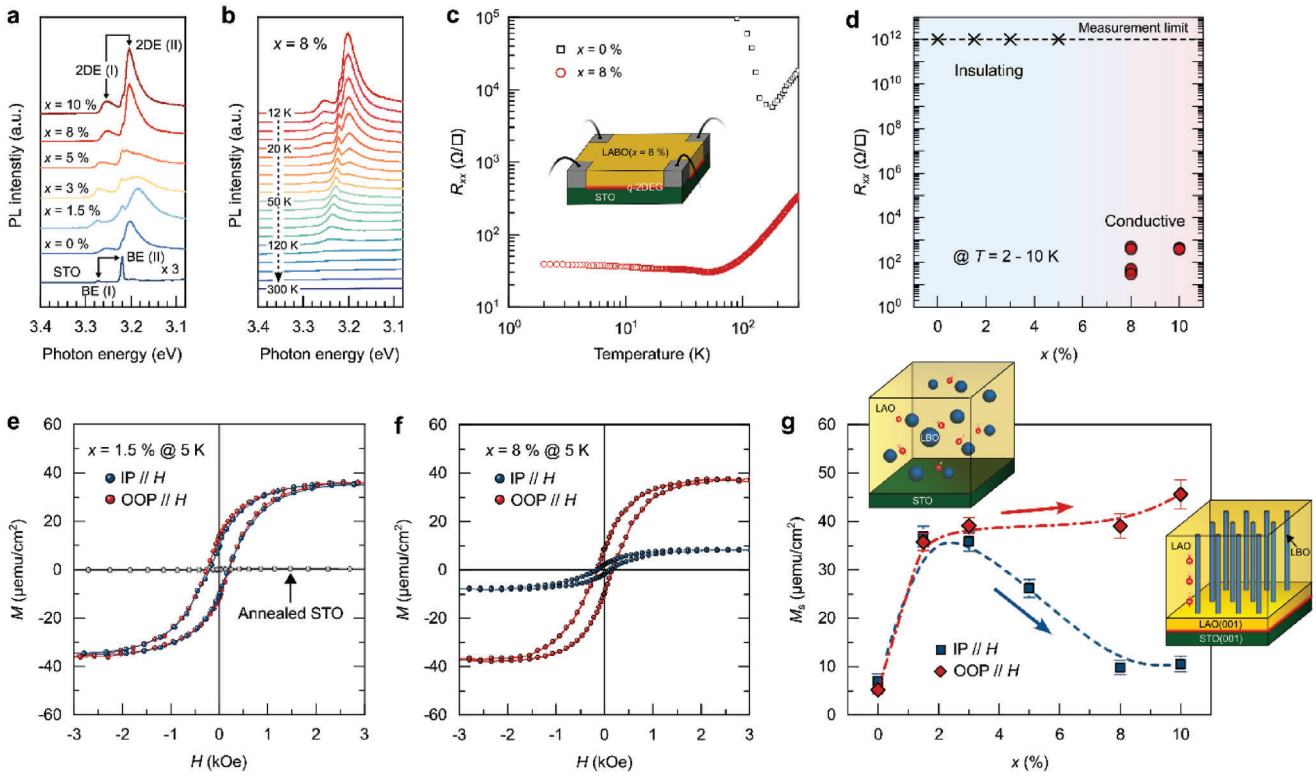

Figure 4. The co-existence of 2DEG and out-of-plane magnetic ordering in the 2D–3D LABO/STO(001) heterostructure. a) Near BE PL spectra of the LABO(x = 1.5%, 3%, 5%, 8%, and 10%) nanocomposite films grown on STO, measured at 12 K. The BE of the undoped LAO/STO and LABO/STO samples show additional emission besides the BE (I & II) peaks of STO, which are assigned to the emission peaks of the 2DEG (I & II). b) Variable temperature (12 – 300 K) near BE spectra of the LABO (x = 8%) / STO sample. c) Temperature-dependent sheet dc-resistance (R_{xx}) of ≈25 nm-thick undoped LAO/STO and ≈24 nm-thick LABO (x = 8%)/STO samples, measured in the Van der Pauw geometry. d) Low temperature (2 – 10 K) R_{xx} of the LABO/STO samples as a function of x (0% – 10%). e) The 5 K IP and OOP magnetic hysteresis loops of the LABO (x = 1.5%)/STO sample. f) The 5 K IP and OOP magnetic hysteresis loops of the LABO (x = 8%)/STO sample. For clarity, the presented magnetic data have been corrected by subtracting the background DM and PM components caused by instrumental accessories and the substrate (Figure S8, Supporting Information). g) Variations in the IP and OOP M_s of the LABO/STO samples as a function of x (0% – 10%). The identical IP and OOP magnetic responses respond to randomly distributed magnets in the film as schematically illustrated in the inset. While, larger (× ≈ 4.5) OOP M_s of the samples was found compared to the IP ones, corresponding to preferential OOP magnetic orderings in the 3D-VAN LABO film structure.

composition increases to x = 8 and 10%, both of the LABO/STO heterostructures exhibit metallic behaviors with decreasing the sheet resistance (R_{xx}) upon cooling (Figure 4c). This confirms the formation of 2DEGs at their LAO(001)$_{pc}$/STO(001) interfaces as illustrated in Figure 4d.

Another intriguing observation is the appearance of magnetism with its anisotropic nature, which is accompanied with the development of the 2D–3D LABO/STO heterostructures. In this work, all the measured magnetic hysteresis loops were carefully evaluated (see Experimental Section and Figure S8, Supporting Information). For clarity, the presented magnetic data have been corrected by subtracting the background diamagnetic (DM) and paramagnetic (PM) components caused by instrumental accessories and the substrate. No ferromagnetic responses were found in an annealed TiO_2-STO substrate used for film growth and the undoped LAO and LBO bulk materials used for film deposition (see Figure 4e and Figures S8 and S9, Supporting Information). Note that the magnetic moment per surface area (M) is used in this study considering the uncertainty in quantitatively determining the B contents, their positions within the samples (e.g., VAN film layers) and the thickness of the films. The undoped LAO/STO heterostructure shows a typical low saturation magnetization (M_s) of M = 4 – 7 μemu cm^{-2}, measured along both the in-plane [IP, H//(100)] and out-of-plane [OOP, H//(001)] directions at 5 K (Figure S9, Supporting Information).

Figure 4e illustrates the 5 K IP and OOP magnetic hysteresis loops of the LABO/STO sample with the LBO composition of x = 1.5% (like a solid solution). Clear ferromagnetic hysteresis loops of the sample were found with no variation in the IP and OOP saturation magnetization of ≈37 μemu cm^{-2}. In contrast, a large difference was observed for $x \geq$ 8%, i.e., the OOP M_s of the LABO(x = 8%)/STO was found to be ≈30 μemu cm^{-2} in comparison with about 6 μemu cm^{-2} for the IP magnetization (Figure 4f). The OOP saturation magnetization of the 2D–3D LABO($x \geq$ 8%)/STO samples was found to be about 5 times stronger than the IP magnetization. The results indicate that the magnetic anisotropy is due to the formation of vertically aligned LABO structure (i.e., a large difference between the IP and OOP magnetization, IP-M_s < OOP-M_s). Conversely, no magnetic anisotropy was observed in the LABO(x = 1.5 and 3%)/STO structures. This indicates that the development of VAN-LABO structure which is associated with the strain relaxation

(2D-to-3D transition) process plays a role in creating a preferential out-of-plane (OOP) magnetism. The values of the measured IP and OOP M_s are listed in Figure 4g and Figure S10 (Supporting Information).

The strong preferential magnetization observed in the OOP of vertically aligned LABO structure is different from the low magnetization of the undoped LAO/STO interfaces (e.g., oxygen defect-mediated magnetic ordering and/or localized unpaired Ti *d*-band electron spins through exchange coupling of itinerant carriers), which is typically expected to show an in-plane ordering of the magnetic domains.[16] Experimentally, the LAO/STO systems with oxygen vacancies usually show relatively small saturation magnetic moments, e.g., in the range of $m_s \approx 1 - 4 \times 10^{12}$ μ_B mm^{-2}).[11,37–40] The magnetic responses of the LABO nanocomposite correspond to an OOP saturation magnetic density of $\approx 3.5–4.75 \times 10^{13}$ μ_B mm^{-2} for the 5×5 mm^2-sized LABO sample ($x \geq 8\%$) and the in-plane density of $\approx 8 \times 10^{12}$ μ_B mm^{-2}, similar to typical moment density ($\approx 10^{12}$ μ_B mm^{-2}) of stoichiometric LAO/STO interfaces reported in the literature.[37] Our results indicate that the magnetization of the LABO/STO heterostructures does not increase with increasing *x*, implying that there is no direct contribution of LBO on the magnetism of the nanocomposite films (Figure S9, Supporting Information). Hence, we suggest that the origin of magnetism in the LABO nanocomposite system is associated with the boron interstitials (B_i).[30] Interstitial B doping can transform the non-magnetic host oxide into a high-temperature ferromagnetism as an impurity band-associated Stoner ferromagnetism.[41] Our theoretical calculation, include $3 \times 3 \times 3$ supercell structures which consist of 27 LAO UCs (135 atoms). B_i contribute to the total excessive charge with about 0.99 e of spin-polarized electrons which are transferred predominantly to the neighboring La atoms of the LAO through the *p–d* band hybridization. This results in a total magnetization moment of 1 μ_B per LAO UC. Additionally, theoretical calculations carried out in this work show that the effective B_i doping in the host LAO lattices is limited to 3.2 at.% due to the tendency of dimerization/clustering. We confirmed that the effect of oxygen vacancies on the boron interstitial-induced ferromagnetism is negligible. The effect of B_i doping on the magnetization of LAO in the LABO system was experimentally confirmed, e.g., B_i diffuse out from the LABO composite during the post-annealing (e.g., $T_A = 600$ °C), resulting in the loss of B_i and the subsequent decrease in the magnetization of the LABO system.[30] Furthermore, when a ≈10 nm-thick amorphous LBO film is deposited on a LAO single crystal substrate even at room temperature, a diffusive B characteristic and the following B_i-induced magnetism have been also observed (Figure S9, Supporting Information). This unique B_i-induced magnetism is not only limited to the LAO system and the effect could be extended to various other dielectric materials, e.g., by ensuring difference in the electronegativity between the cation and anion in host materials and by implanting and ordering the B_i in various dielectric/ferroelectric materials.[30]

We therefore postulate that the distribution/orderings of B_i in the host LAO lattices could be located near the vertical LAO/LBO interfaces to release the vertical interface energy for stabilizing the VAN system[20,23,42,43] although a precise atomic identification of B_i position is still challenging. Nonetheless, it was possible to confirm the presence of metallic B_i in the local area of a 3D LABO nanocomposite layer by STEM-EELS (**Figure 5**a,b) and NMR (Figure S11, Supporting Information). In the STEM-EELS spectra, two weak energy loss peaks were found at ≈194 and ≈202.5 eV for B_2O_3, typically resulting from the transition of a 1*s* electron to unoccupied B-O π^* and σ^*antibonding orbitals, respectively.[44] In the upper 3D film layer, an anomalous peak between the π^* and σ^* peaks is dominated at ≈195.8 eV, which could be associated with the lowered energy of σ^* peak due to the loss of LBO symmetry in the 3D-LABO strain network.[44,45] Besides these, in the 3D film layer, a peak at ≈187 eV visibly appears, which reflects the existence of metallic B_i.[30] Based on these observations, the magnetic anisotropy is correlated with preferential B_i ordering in the VAN structure formation: i) no magnetism observed in the undoped LAO and the LBO (Figure S9, Supporting Information), ii) the creation of magnetism exists only in the presence of B_i, iii) preferential OOP magnetization observed only for the VAN-LABO structure, iv) VAN-LABO film formation with vertical interfaces, and v) the indication of higher B_i concentration near the vertical interface toward the neighboring LAO lattice.

To understand the above magnetic nature in the LABO films, we performed first principles calculations on strained LAO supercells with B_i. First, there is no effect of substitutional B doping on the creation of magnetism in a tetragonally distorted LAO (by replacing B-site Al cation with B) and no magnetism in a tetragonally deformed LBO structure. Next, to study the preferential magnetic structure, we simulated boron impurities in a 3%-biaxial strained LAO (Figure 5c). This model mimics the lattice mismatch between LAO and STO and the initial growth of LAO overlayer which is tetragonally compressed, so that the La-B-La chains are not equivalent. The in-plane (IP) chains expand in this regime, however, together with a significant relaxation of the four nearest oxygens to B_i, it shows relatively very weak total magnetization (m_B and $m_{La} < 0.02$ μ_B) (Figure 5d). In contrast, when a B_i is energetically relaxed in the middle of two La atoms along the OOP direction of the LAO induces the total magnetic moment up to 1 μ_B (e.g., $m_B = 0.4$ μ_B for B_i and $m_{La} = 0.2$ μ_B for La) (Figure 5e). Thus, the OOP La-B_i-La chains form as magnetic species in the B_i-doped LAO. Figure 5f shows that the B_i induces three impurity bands: two spin-up and one spin-down peaks which are situated just below the Fermi level (E_F) in the bandgap of the LAO. The calculated spin imbalance is +1 that enables the magnetization of 1 μ_B in the system. It should be noted that the total magnetic moment of LAO induced by a B_i cannot exceed 1 μ_B because it is induced by *n*-doping with one extra electron of B_i. In our experiment, the OOP magnetic moment of the LABO film samples is found to be ≈10 μemu, corresponding to $\approx 1.08 \times 10^{15}$ μ_B. Based on the theoretically calculated moment of 1 μ_B per B_i and assuming that all the B_i are accumulated along the vertical LAO/LBO interfaces, the B_i doping can induce effective moment of ≈0.7 – ≈1.02 μ_B/B_i in a 20 nm-thick VAN-LABO ($x = 10\%$) as given in Table S1 (Supporting Information). Hence, the above *ab-initio* calculations support the observed preferential magnetic order along the OOP direction of the LABO film layer.

3. Conclusion

In this work, we demonstrate a self-assembly of combined 2D and 3D nanocomposite heterostructure, which can be evoked

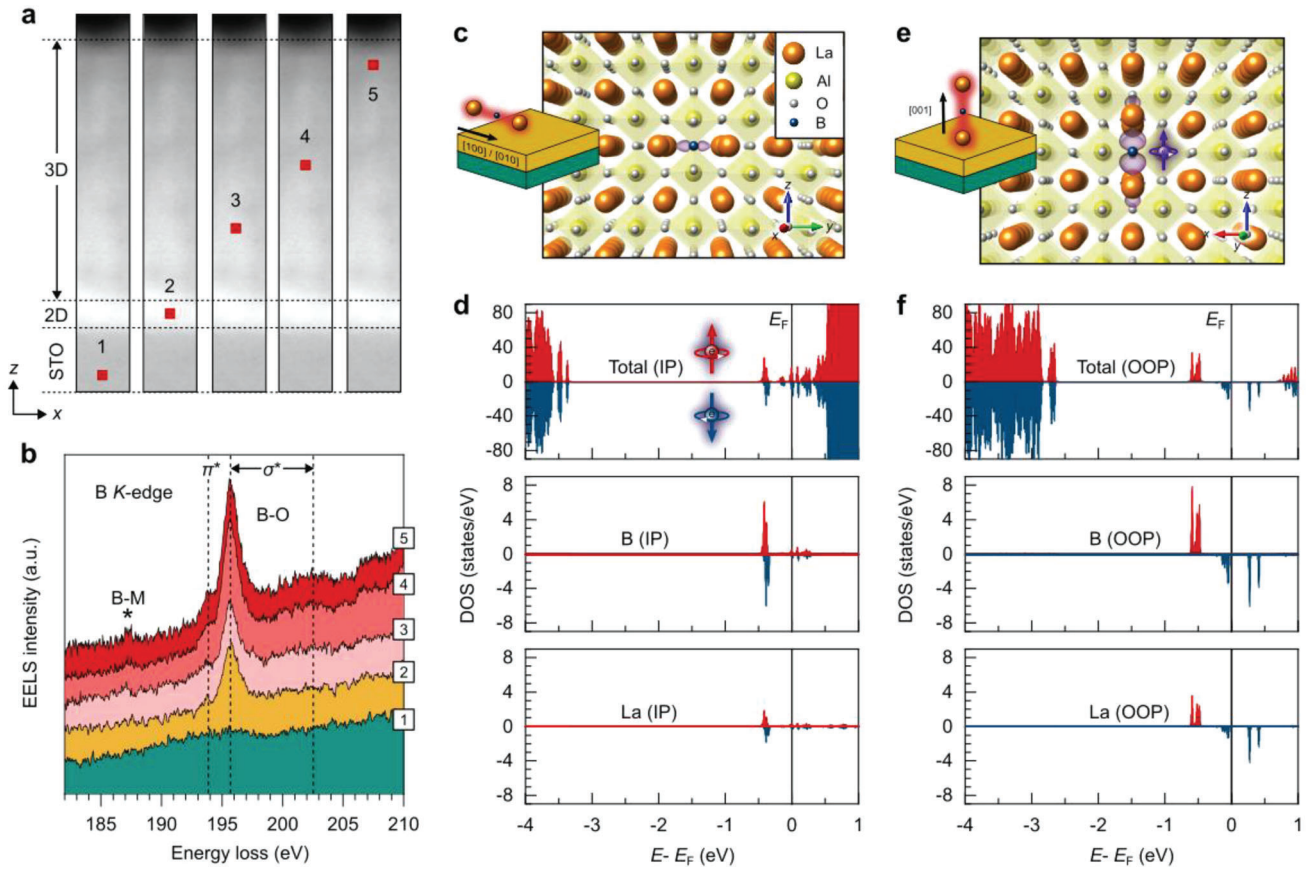

Figure 5. The B_i-associated magnetism in the LABO system. a) Selected points (1 – 5) in the same local area of a LABO (x = 10%)/STO heterostructure for B K-edge EELS spectra acquisition. b) The corresponding experimental EELS spectra from a top area of STO (1) to a top area of the 3D LABO layer (5). c) Magnetization density of the 3%-strained LAO induced by an IP La-B-La chain. d) Spin-polarized density of states (DOS) of the B-doped LAO with the IP La-B-La chain: the top panel is the total DOS, the middle one is the B-projected DOS, the bottom panel is the partial DOS of the nearest La neighbor. e) Magnetization density of the strained LAO induced by an OOP La-B-La chain. f) Spin-polarized density of states (DOS) of the B-doped LAO with the OOP La-B-La chain.

by the composition of two constituent oxide phases. To achieve this structural transition, it is essential to control the ratio between two phases, LAO and LBO. In order to achieve the initial 2D LAO layer and the subsequent 3D LABO layer, it is required that the host LAO composition should be higher than that of the LBO. Thus, finding an appropriate composition of LBO is a key parameter for driving the spontaneous transition from 2D to 3D-VAN LABO/STO(001) structure – in this work, the structural transition happened at the composition of $x \geq 8\%$. The underlying mechanism for the transient formation of the 2D-to-3D VAN LABO/STO(001) structure is associated with the misfit strain-mediated phase separation of miscible LAO and LBO oxide phases in conjunction with strain relaxation processes: i) at the initial growth stage, the tensile-strained B:LAO monolayer is formed on STO, ii) the horizontal elastic energy increases with film thickness, iii) B diffuses into energetically favorable sites (e.g., edge dislocations) to relieve the strain energy, and iv) the nucleation and growth of LBO phase in the host LAO matrix. This self-assembly approach is different with the pervious observation of YBCO:BZO composite.[23] For the LABO VAN formation, the structure of LBO is highly anisotropic and thus can be vertically matched with highly stiff LAO (c_{11} ≈308 GPa).[46] Moreover, the creation and percolation of B interstitials into the neighboring LAO lattice across the vertical LAO/LBO interfaces could be associated with a release in the vertical strain energy for stabilizing the composite system. Such a transition from 2D to 3D–VAN structure observed in the current study is characterized by unique strain orderings, which are strongly coupled with the 2D electron gas at the planar interface between the STO and the LAO and the preferential magnetic ordering at the vertical interfaces when the 3D VAN structure is formed. Thus, the 2D–3D VAN LABO/STO structure has the following advantages: i) self-assembly structure, ii) surpassing the thickness limit of continuous horizontal 2DEG-LAO/STO interface without microcracks, and iii) magnetic VAN structure with perpendicular magnetic ordering. This provides unique heterostructures which include both the 2DEG and magnetism in a single film. Our work offers new perspectives for designing and controlling the magnetic and electric properties at the interfaces of complex oxide nanocomposite thin film heterostructures via a self-assembly approach. This self-assembly approach is a powerful means not only for nanoscale investigation of emerging physics phenomena, but also it could extend engineering of thin film materials beyond the current limits of atomically delicate interface engineering.

4. Experimental Section

Sample Preparation: For PLD film growth, LABO(x) ceramic targets were fabricated by standard solid-state synthesis techniques by mixing three different metal oxide powders (highly pure 99.99% – 99.999% La_2O_3, Al_2O_3, and B_2O_3 powers). The mixed and pressed targets were sintered at 1400 °C for 4 h in air.[30] LABO films ($x = 0 - 10\%$) were grown on TiO_2-$SrTiO_3$(001) using PLD (KrF excimer laser: $\lambda = 248$ nm). The growth temperature was kept constant at 700 °C and the films were grown under oxygen partial pressure of $5 \times 10^{-4} - 1 \times 10^{-3}$ mbar. After film growth, all the samples were cooled down to room temperature at the same growth pressure with a ramping-down rate of 10 °C min^{-1}. The films were grown by a laser fluence of ≈1.6 J cm^{-2} with a repetition rate of 1 Hz. The growth characteristics and thickness of all the films were monitored and controlled by reflection of high energy electron diffraction (RHEED). All the film preparations were carried out in different PLD laboratories in UK, South Korea, and Germany.

Sample Characterizations: Structural properties of all the grown films were examined by a high-resolution Bruker D8 Discover diffractometer with monochromatic Cu Kα1 radiation (λ = 1.54056 Å). The magnetic measurements were performed by Quantum Design SQUID Magnetometer with the samples mounted at different orientations to measure the in-plane [100] and out-of-plane [001] crystallographic directions. To evaluate the magnetic properties of the films, external magnetic contributions were eliminated by measuring the sample holders and accessories (low-temperature glues). The substrate contribution was subtracted from the field-dependent magnetization data by removing a field-linear diamagnetic term fitted to the high-field data (Figure S8, Supporting Information). Microstructural properties of the LABO films were determined by performing scanning electron microscopy (a FEI double Cs-aberration corrected Titan3 G2 60–300 S/TEM instrument with Chemi-STEM technology). For ^{11}B NMR, The LABO-STO thin films were sliced into sub-mm pieces and packed into rotors. No grinding was performed on the samples, to ensure that degradation of the samples did not take place. To make the samples spin stably, PTFE tape was inserted into each rotor to fill the void space left by such inefficient packing. There was possible evidence of preferential alignment features in the solid-state NMR results achieved, this suggested the boron had a preferred alignment in the thin film. All ^{11}B ($I = 3/2$) MAS (12 kHz) solid-state NMR spectra were achieved using a 11.7T Bruker Avance III 500 MHz spectrometer operating at a Larmor frequency of 160.45 MHz. A Varian-Chemagnetics 4 mm probe was utilized to achieve spinning frequencies of 12 kHz and to prevent a boron background being visible. The single pulse experiment consisted of a "non-selective" (solid) $\pi/6$ pulse of 1.0 µs pulse. The spectra were calibrated to the secondary reference $NaBH_4$ ($\delta_{iso} = -42.09$ ppm w.r.t $BF_3.Et_2O$ in $CDCl_3$ at 0 ppm).[47] The T_1 data was simulated to a single exponential, $f(t) = I_0.[1\text{-}\exp(\text{-}t/T_1)]$, and no statistically significant improvements were achieved with stretched or multiple exponential simulations. As the T_1 relaxation of the B_i environment was measured at 0.522 seconds, all experiments were taken with a 60° nutation tip angle and $3 \times T_1$ to achieve maximum efficiency of the experiment. All spectral simulations were completed using the in-house developed Quadfit program.[48] Photoluminescence data for the samples were collected at variable temperatures (5–300 K) using an excitation energy of HeCd laser (λ = 325 nm). A complementary long-pass optical filter with a cut-off wavelength of 420 nm was used to increase the dynamic range of deep level emissions in the samples and remove the laser line and its second-order diffraction. All the PL measurements were performed using a constant optimized exposure for the absolute comparison of the luminescence intensity from the samples. For the electrical measurements, the measured sample sizes were 5×5 mm^2 and 2.5×5 mm^2 and contracts were achieved by Ohmic Al wire bonding on all the edge corners of the sample. The transport measurements were carried out in a CRYOGENIC cryogen-free measurement system with the temperature ranging from RT to 4 K. The temperature was controlled utilizing a Lakeshore 340. Measurements were done utilizing a SR830 lock-in amplifier with a 300 MΩ load resistor at a frequency of 77.39 Hz and a voltage excitation of 3 V for 10 nA driving current.

Theoretical Calculations: The density functional theory (DFT) package VASP[49] was used to calculate the electronic, structural, and magnetic properties of LAO doped by boron. The code had a plane-wave basis set that provides the reliable structural optimizations and accurate energetics. Electron-ion interactions within VASP calculations were described by projector-augmented wave pseudopotentials and electronic wave functions were represented by plane waves with an energy cutoff of 450 eV. The Perdew-Burke-Ernzerhof (PBE) generalized-gradient approximation (GGA)[50] to the exchange-correlation potential was used here. The use of GGA-PBE and its reliability were discussed previously for simulations of the LAO overlayers on $SrTiO_3$(001)[11,51] and boron-doped material.[30] The equilibrium lattice parameter of LAO, which was obtained within the GGA-PBE, was 3.79 Å. Here, by adding one boron into the 135-atom LAO supercell, an isolated B impurity was simulated in cubic and tetragonally distorted LAO and tetragonally distorted LBO. In all cases, the positions of boron and its nearest cations and oxygens were allowed to relax. The structural relaxation was performed using the $4 \times 4 \times 4$ **k**-mesh and the conjugate-gradient algorithm until the Hellmann–Feynman forces became less than 5×10^{-3} eV Å^{-1}. The density of states (DOS) was obtained then using the Γ-centered and compacted **k**-mesh with minor smearing of 10 meV. The DOS calculations were performed also in the presence of the spin-orbital coupling (SOC), within the non-collinear option of VASP.[52]

Supporting Information

Supporting Information is available from the Wiley Online Library or from the author.

Acknowledgements

The authors thank E. B. Þorsteinsson in the University of Iceland, Iceland, for his technical support for this work. Dr. K. Kaufmann in Fraunhofer Center for Silicon Photovoltaics, Germany, is thanked for his support on the elementary analysis of samples. Authors thank Dr. M. Walker in the University of Warwick for XPS measurements. Dr. A. Bhatnagar in Zentrum für Innovationskompetenz SiLi-nano, Germany, is thanked for useful discussion on this work. D.-S.P. and N.P. acknowledge the support from the European Commission through project Biowings H2020 FET-OPEN 2018–2022 (grant No 80127). D.-S.P. acknowledges the funding from Villum Fonden (SYMTEC, grant No 111814). Y.L.G. acknowledges the support from China Postdoctoral Science Foundation (grant No 2020M680726, YJ20200325). N.P. acknowledges funding from Villum Fonden for the NEED project (grant No 00027993), the Danish Council for Independent Research Technology and Production Sciences for the DFF- Research Project 3 (grant No 00069B) the "Challenge Programme 2021 – Smart Nanomaterials for Applications in Life-Science" Grant No. NNF21OC0066526 and the funding from the ERC Advanced "NEXUS" Grant 101054572. W.S.C. was supported by the National Research Foundation of Korea (grant No NRF-2021R1A2C2011340). F.T. acknowledges the support by research grant 37338 (SANSIT) from Villum Fonden.

Conflict of Interest

The authors declare no conflict of interest.

Data Availability Statement

The data that support the findings of this study are available in the supplementary material of this article.

Keywords

2DEGs, functional oxides, magnetism, self-assembly, thin film growth

Received: January 7, 2023
Revised: May 1, 2023
Published online:

[1] A. Ohtomo, H. Y. Hwang, *Nature* **2004**, *427*, 423.
[2] Y. Zhou, X. Guan, H. Zhou, K. Ramadoss, S. Adam, H. Liu, S. Lee, J. Shi, M. Tsuchiya, D. D. Fong, S. Ramanathan, *Nature* **2016**, *534*, 231.
[3] J. Chakhalian, X. Liu, G. A. Fiete, *APL Mater.* **2020**, *8*, 050904.
[4] D. V. Efremov, J. V. D. Brink, D. I. Khomskii, *Nat. Mater.* **2004**, *3*, 853.
[5] T. Taniuchi, Y. Motoyui, K. Morozumi, T. C. Rödel, F. Fortuna, A. F. Santander-Syro, S. Shin, *Nat. Commun.* **2016**, *7*, 11781.
[6] C. Ederer, N. A. Spaldin, *Nat. Mater.* **2004**, *3*, 849.
[7] H. Zheng, J. Wang, S. E. Lofland, Z. Ma, L. Mohaddes-Ardabili, T. Zhao, L. Salamanca-Riba, S. R. Shinde, S. B. Ogale, F. Bai, D. Viehland, Y. Jia, D. G. Schlom, M. Wuttig, A. Roytburd, R. Ramesh, *Science* **2004**, *303*, 661.
[8] N. Reyren, S. Thiel, A. D. Caviglia, L. Fitting Kourkoutis, G. Hammerl, C. Richter, C. W. Schneider, T. Kopp, A.-S. Rüetschi, D. Jaccard, M. Gabay, D. A. Muller, J.-M. Triscone, J. Mannhart, *Science* **2007**, *317*, 1196.
[9] L. Li, J. Mannhart, R. C. Aschoori, *Nat. Phys.* **2011**, *7*, 762.
[10] J. W. Park, D. F. Bogorin, C. Cen, D. A. Felker, Y. Zhang, C. T. Nelson, C. W. Bark, C. M. Folkman, X. Q. Pan, M. S. Rzchowski, J. Levy, C. B. Eom, *Nat. Commun.* **2010**, *1*, 94.
[11] D.-S. Park, A. D. Rata, I. V. Maznichenko, S. Ostanin, Y. L. Gan, S. Agrestini, G. J. Rees, M. Walker, J. Li, J. Herrero-Martin, G. Singh, Z. Luo, A. Bhatnagar, Y. Z. Chen, V. Tileli, P. Muralt, A. Kalaboukhov, I. Mertig, K. Dörr, A. Ernst, N. Pryds, *Nat. Commun.* **2020**, *11*, 3650.
[12] Y. Chen, N. Pryds, J. E. Kleibeuker, G. Koster, J. Sun, E. Stamate, B. Shen, G. Rijnders, S. Linderoth, *Nano Lett.* **2011**, *11*, 3774.
[13] M. P. Warusawithana, C. Richter, J. A. Mundy, P. Roy, J. Ludwig, S. Paetel, T. Heeg, A. A. Pawlicki, L. F. Kourkoutis, M. Zheng, M. Lee, B. Mulcahy, W. Zander, Y. Zhu, J. Schubert, J. N. Eckstein, D. A. Muller, C. S. Hellberg, J. Mannhart, D. G. Schlom, *Nat. Commun.* **2013**, *4*, 2351.
[14] M. Salluzzo, S. Gariglio, X. Torrelles, Z. Ristic, R. Di Capua, J. Drnec, M. Moretti Sala, G. Ghiringhelli, R. Felici, N. B. Brookes, *Adv. Mater.* **2013**, *25*, 2333.
[15] S. Zeng, W. Lü, Z. Huang, Z. Liu, K. Han, K. Gopinadhan, C. Li, R. Guo, W. Zhou, H. H. Ma, L. Jian, T. Venkatesan, Ariando, *ACS Nano* **2016**, *10*, 4532.
[16] F. Bi, M. Huang, S. Ryu, H. Lee, C.-W. Bark, C.-B. Eom, P. Irvin, J. Levy, *Nat. Commun.* **2014**, *5*, 5019.
[17] D. Stornaiuolo, C. Cantoni, G. M. De Luca, R. Di Capua, E. Di Gennaro, G. Ghiringhelli, B. Jouault, D. Marrè, D. Massarotti, F. M. Granozio, I. Pallecchi, C. Piamonteze, S. Rusponi, F. Tafuri, M. Salluzzo, *Nat. Mater.* **2015**, *15*, 278.
[18] D. N. Ngo, J.-W. Chang, K. Lee, S. Han, J. S. Lee, Y. H. Kim, M.-H. Jung, Y.-J. Doh, M.-S. Choi, J. Song, J. Kim, *Nat. Commun.* **2015**, *6*, 8035.
[19] V. T. Tra, J.-W. Chen, P.-C. Huang, B.-C. Huang, Y. Cao, C.-H. Yeh, H.-J. Liu, E. A. Eliseev, A. N. Morozovska, J.-Y. Lin, Y.-C. Chen, M.-W. Chu, P.-W. Chiu, Y.-P. Chiu, L.-Q. Chen, C.-L. Wu, Y.-H. Chu, *Adv. Mater.* **2013**, *25*, 3357.
[20] J. L. MacManus-Driscoll, P. Zerrer, H. Wang, H. Yang, J. Yoon, A. Fouchet, R. Yu, M. G. Blamire, Q. Jia, *Nat. Mater.* **2008**, *7*, 314.
[21] J. L. MacManus-Driscoll, A. Suwardi, H. Wang, *MRS Bull.* **2015**, *40*, 933.
[22] H. Zheng, F. Straub, Q. Zhan, P.-L. Yang, W.-K. Hsieh, F. Zavaliche, Y.-H. Chu, U. Dahmen, R. Ramesh, *Adv. Mater.* **2006**, *18*, 2747.
[23] R. Zhao, W. Li, J. H. Lee, E. M. Choi, Y. Liang, W. Zhang, R. Tang, H. Wang, Q. Jia, J. L. MacManus-Driscoll, H. Yang, *Adv. Funct. Mater.* **2014**, *24*, 5240.
[24] X. Gao, L. Li, J. Jian, J. Huang, X. Sun, D. Zhang, H. Wang, *Appl. Phys. Lett.* **2019**, *115*, 053103.
[25] M. Ohring, *Materials Science of Thin Films*, Academic Press, Cambridge **2002**.
[26] S. M. Yang, S. Lee, J. Jian, W. Zhang, P. Lu, Q. Jia, H. Wang, T. W. Noh, S. V. Kalinin, J. L. MacManus-Driscoll, *Nat. Commun.* **2015**, *6*, 8588.
[27] S. A. Harrington, J. Zhai, S. Denev, V. Gopalan, H. Wang, Z. Bi, S. A. T. Redfern, S.-H. Baek, C. W. Bark, C.-B. Eom, Q. Jia, M. E. Vickers, J. L. MacManus-Driscoll, *Nat. Nanotechnol.* **2011**, *6*, 491.
[28] C. Cancellieri, D. Fontaine, S. Gariglio, N. Reyren, A. D. Caviglia, A. Fête, S. J. Leake, S. A. Pauli, P. R. Willmott, M. Stengel, Ph. Ghosez, J.-M. Triscone, *Phys. Rev. Lett.* **2011**, *107*, 056102.
[29] E. M. Levin, R. S. Roth, J. B. Martin, *Am. Mineral* **1961**, *46*, 1030.
[30] D.-S. Park, G. J. Rees, H. Wang, D. Rata, A. J. Morris, I. V. Maznichenko, S. Ostanin, A. Bhatnagar, C.-J. Choi, R. D. B. Jónsson, K. Kaufmann, R. Kashtiban, M. Walker, C.-T. Chiang, E. B. Thorsteinsson, Z. Luo, I.-S. Park, J. V. Hanna, I. Mertig, K. Dörr, H. P. Gíslason, C. F. McConville, *Adv. Mater.* **2018**, *30*, 1802025.
[31] J. W. Matthews, A. E. Blakeslee, *J. Cryst. Growth* **1974**, *27*, 118.
[32] T. Sluka, A. K. Tagantsev, P. Bednyakov, N. Setter, *Nat. Commun.* **2013**, *4*, 1808.
[33] P. W. Lee, V. N. Singh, G. Y. Guo, H.-J. Liu, J.-C. Lin, Y.-H. Chu, C. H. Chen, M.-W. Chu, *Nat. Commun.* **2016**, *7*, 12773.
[34] M. Stengel, *Phys. Rev. Lett.* **2011**, *106*, 136803.
[35] D. Kan, T. Terashima, R. Kanda, A. Masuno, K. Tanaka, S. Chu, H. Kan, A. Ishizumi, Y. Kanemitsu, Y. Shimakawa, M. Takano, *Nat. Mater.* **2005**, *4*, 816.
[36] M. A. Islam, D. Saldana-Greco, Z. Gu, F. Wang, E. Breckenfeld, Q. Lei, R. Xu, C. J. Hawley, X. X. Xi, L. W. Martin, A. M. Rappe, J. E. Spanier, *Nano Lett.* **2016**, *16*, 681.
[37] Ariando, X. Wang, G. Baskaran, Z. Q. Liu, J. Huijben, J. B. Yi, A. Annadi, A. Roy Barman, A. Rusydi, S. Dhar, Y. P. Feng, J. Ding, H. Hilgenkamp, T. Venkatesan, *Nat. Commun.* **2011**, *2*, 188.
[38] M. Salluzzo, S. Gariglio, D. Stornaiuolo, V. Sessi, S. Rusponi, C. Piamonteze, G. M. De Luca, M. Minola, D. Marré, A. Gadaleta, H. Brune, F. Nolting, N. B. Brookes, G. Ghiringhelli, *Phys. Rev. Lett.* **2013**, *111*, 087204.
[39] B. Kalisky, J. A. Bert, B. B. Klopfer, C. Bell, H. K. Sato, M. Hosoda, Y. Hikita, H. Y. Hwang, K. A. Moler, *Nat. Commun.* **2012**, *3*, 922.
[40] H.-L. Hu, D. Wang, A. Tseng, Z. Chen, C. Kong, J. Yi, S. Li, *Adv. Mater. Interfaces* **2018**, *5*, 1800352.
[41] K. Ackland, M. Venkatesan, J. M. D. Coey, *J. Appl. Phys.* **2012**, *111*, 07A322.
[42] N. Pyds, V. Esposito, *J Electroceram* **2017**, *38*, 1.
[43] S. Hong, S. M. Nakhmanson, D. D. Fong, *Rep Prog Phys* **2016**, *79*, 076501.
[44] S. K. Lee, Y.-H. Kim, P. Chow, Y. Xiao, C. Ji, G. Shen, *Proc. Natl. Acad. Sci. USA.* **2018**, *115*, 5855.
[45] O. Cretu, Y.-C. Lin, M. Koshino, L. H. G. Tizei, Z. Liu, K. Suenaga, *Phys. Rev. Lett.* **2015**, *114*, 075502.
[46] X. Luo, B. Wang, *J. Appl. Phys.* **2008**, *104*, 073518.
[47] R. K. Harris, E. D. A. Becker, *Magn. Reson. Chem.* **2002**, *40*, 489.
[48] T. F. Kemp, M. E. Smith, *Solid State Nucl. Magn. Reson.* **2009**, *35*, 243.
[49] G. Kresse, J. Furthmüller, *Phys. Rev. B* **1996**, *54*, 11169.
[50] J. P. Perdew, K. Burke, M. Ernzerhof, *Phys. Rev. Lett.* **1996**, *77*, 3865.
[51] I. Maznichenko, S. Ostanin, A. Ernst, I. Mertig, *Phys. Rev. Mater.* **2019**, *3*, 074006.
[52] D. Hobbs, G. Kresse, J. Hafner, *Phys. Rev. B* **2000**, *62*, 11556.